

Nonspherical particles in a pseudo-2D fluidized bed

Experimental study

Mahajan, Vinay V.; Padding, Johan T.; Nijssen, Tim M.J.; Buist, Kay A.; Kuipers, J. A.M.

DOI

[10.1002/aic.16078](https://doi.org/10.1002/aic.16078)

Publication date

2018

Document Version

Final published version

Published in

AICHE Journal

Citation (APA)

Mahajan, V. V., Padding, J. T., Nijssen, T. M. J., Buist, K. A., & Kuipers, J. A. M. (2018). Nonspherical particles in a pseudo-2D fluidized bed: Experimental study. *AICHE Journal*, *64*(5), 1573-1590. <https://doi.org/10.1002/aic.16078>

Important note

To cite this publication, please use the final published version (if applicable). Please check the document version above.

Copyright

Other than for strictly personal use, it is not permitted to download, forward or distribute the text or part of it, without the consent of the author(s) and/or copyright holder(s), unless the work is under an open content license such as Creative Commons.

Takedown policy

Please contact us and provide details if you believe this document breaches copyrights. We will remove access to the work immediately and investigate your claim.

Nonspherical Particles in a Pseudo-2D Fluidized Bed: Experimental Study

Vinay V. Mahajan and Johan T. Padding 

Dept. of Process and Energy, Delft University of Technology, 2628 CB Delft, The Netherlands

Tim M. J. Nijssen, Kay A. Buist , and J. A. M. Kuipers

Dept. of Chemical Engineering & Chemistry, Multiphase Reactors Group, Eindhoven University of Technology, 5600 MB Eindhoven, The Netherlands

DOI 10.1002/aic.16078

Published online February 6, 2018 in Wiley Online Library (wileyonlinelibrary.com)

Fluidization is widely used in industries and has been extensively studied, both experimentally and theoretically, in the past. However, most of these studies focus on spherical particles while in practice granules are rarely spherical. Particle shape can have a significant effect on fluidization characteristics. It is therefore important to study the effect of particle shape on fluidization behavior in detail. In this study, experiments in pseudo-2D fluidized beds are used to characterize the fluidization of spherocylindrical (rod-like) Geldart D particles of aspect ratio 4. Pressure drop and optical measurement methods (Digital Image Analysis, Particle Image Velocimetry, Particle Tracking Velocimetry) are employed to measure bed height, particle orientation, particle circulation, stacking, and coordination number. The commonly used correlations to determine the pressure drop across a bed of nonspherical particles are compared to experiments. Experimental observations and measurements have shown that rod-like particles are prone to interlocking and channeling behavior. Well above the minimum fluidization velocity, vigorous bubbling fluidization is observed, with groups of interlocked particles moving upwards, breaking up, being thrown high in the freeboard region and slowly raining down as dispersed phase. At high flowrates, a circulation pattern develops with particles moving up through the center and down at the walls. Particles tend to orient themselves along the flow direction. © 2018 The Authors AICHE Journal published by Wiley Periodicals, Inc. on behalf of American Institute of Chemical Engineers AICHE J, 64: 1573–1590, 2018

Keywords: fluidization, nonspherical, bed height, pressure drop, orientation, Particle Image Velocimetry, Particle Tracking Velocimetry, Digital Image Analysis

Introduction

Gas-solid fluidized beds are widely employed in many industries due to their favorable mixing, mass- and heat-transfer characteristics. Fluid catalytic cracking, polymerization, drying, and granulation are a few examples of their applications. In recent years, there has been increased application of fluidized beds in biomass gasification and clean energy production.¹ Therefore, understanding of complex dense gas–solid flows is important. Consequently, numerous fundamental studies have been performed in this area. Experimental, theoretical and numerical studies have been used to describe the properties of the fluidized bed. However, almost all research has been conducted using nearly spherical particles because of their geometrical simplicity. In industry, particles are rarely perfectly spherical.² On microscale, particle shape defines the structure of the granular material which contributes massively

to bulk behavior of such systems on macrolevel. The dynamics of nonspherical particles can be very different and more complex as compared to spherical particles. Such particles experience anisotropic drag^{3–5} and anisotropic collisions, both of which depend on local spatial distribution and degree of alignment of neighboring particles and the proximity of internal or external walls. Knowledge about the influence of particle shape is therefore essential, for example for reactor design and optimization.

Over the past few decades, a large number of experimental studies have been performed on fluidized beds containing spherical particles.^{6–8} Nonspherical particle fluidization has been gaining interest in recent years as a field of research.² The focus has mainly been on numerical approaches, with experimental results being available, but scarce. Zhong et al. were among the first to present an experimental study on expansion ratio and pressure drop for rod-like particles.⁹ Vollmari et al. conducted research on the pressure drop and flow regime transitions of a variety of irregularly shaped particles.¹⁰ They found that as particles become more nonspherical, they are harder to fluidize and therefore require higher gas inlet velocities. For very elongated particles, channeling is observed instead of smooth fluidization.¹¹ Liu et al. also conducted experiments and observed poor fluidizing quality as compared to spherical particles.¹² Liu and Litster found that nonspherical

Correspondence concerning this article should be addressed to J. T. Padding at j.t.padding@tudelft.nl.

This is an open access article under the terms of the Creative Commons Attribution-NonCommercial License, which permits use, distribution and reproduction in any medium, provided the original work is properly cited and is not used for commercial purposes.

© 2018 The Authors AICHE Journal published by Wiley Periodicals, Inc. on behalf of American Institute of Chemical Engineers

particles tend to spout, forming high fountains.¹³ Cai et al. studied experimentally the orientation of cylindrical particles in a circulating fluidized bed and found the axes of cylindrical particles aligned upright during fluidization.¹⁴ Very recently, Boyce et al. studied gas, particle velocity and void fraction for fluidization of Kidney-bean-like particles via magnetic resonance imaging.¹⁵ A number of other experimental techniques like Magnetic Particle Tracking, Positron Emission Particle Tracking (PEPT), and Radioactive Particle Tracking have also been used to study such systems.^{16–18} These techniques can be effectively used to study the behavior of particles in the bulk region of the bed. However, these techniques allow for tracking of single or few tracer particles for which quantities are then temporally averaged to get the general behavior of particles in the bed. This does not allow for investigation of the collective motion of particles.

Cofluidization of multiple particle shapes has been investigated as well.¹⁹ Studies on mixing and segregation have shown that differently shaped particles can separate when fluidized, even when their volume and density are similar.²⁰ Experimental studies indicate that sphericity alone is not sufficient to describe the effect of particle shape on fluidization behavior. Multiple shape factors have been proposed to quantify this influence, such as the Zingg factor,¹² the cross-wise and length-wise sphericity,⁴ and the aspect ratio.²¹ Correlations for drag force, pressure drop, and flow-regime transitions based on the aforementioned shape factors were developed, with variable results. Even more so than experimental studies, numerical methods are employed to study nonspherical particle fluidization.¹¹

To further our understanding of such systems, in this study the fluidization of spherocylinder-shaped particles is investigated using an experimental approach. In a pseudo-2D fluidized bed filled with spherocylindrical particles, pressure drop and bed expansion is measured as a function of the gas flow rate. Digital Image Analysis (DIA), Particle Image Velocimetry (PIV), and Particle Tracking Velocimetry (PTV) are used to determine particle coalignment, orientation, circulation patterns, coordination number, and local particle dynamics in the bed. We also demonstrate with experiments the difference in fluidization behavior for rod-like particles as compared to volume equivalent spheres.

Experimental Setup

Experiments are conducted on two different scales with similar setups, to confirm that the observed behavior is truly a property of particle shape, not particle size. The setups are shown schematically in Figure 1, and specifications are given in Table 1. A pseudo-2D fluidized bed with a glass front wall is used. Flow distributors are used to guarantee a flat gas velocity profile entering the bed. A differential pressure sensor (MPX5050DP) is attached at the bottom of the beds to measure pressure drop.

The beds are filled with spherocylindrical particles (schematically shown in Figure 2) up to a packed bed height of approximately the bed width. Particle dimensions are given in Table 1. The particles are made of Alumide, a composite material of nylon and Aluminum dust which is a high strength, low density material. The particles are produced using Selective Laser Sintering (SLS), a 3D printing method. This technique allows for the inexpensive production of small particles, while still maintaining well-defined shape specifications. A number of independent size measurements were performed for a number of randomly selected particles. We found little or no

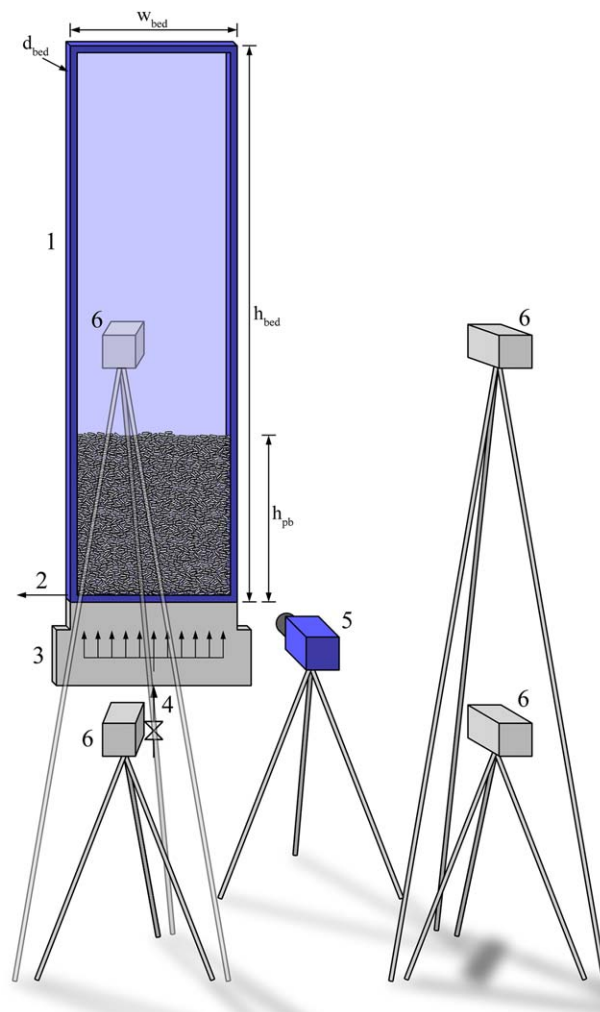


Figure 1. Representation of the setups. The pseudo-2D fluidized bed (1) is filled to a packed bed height of approximately the bed width.

Gas enters through the valve (4). A flow distributor (3) is used to guarantee a flat gas velocity profile entering the bed. Pressure measurements are taken at the bottom of the bed. The camera (5) is positioned in front of the bed, and surrounded by 4 lights (6). Dimensions are given in Table 1. [Color figure can be viewed at wileyonlinelibrary.com]

variation in size (less than 0.1 mm differences). The particle density was measured by weighing 1000 particles using a VWR LPW-713i balance. The resulting measured density was 1395 kg/m³.

Table 1. Dimensions of the Setups (Figure 1) and Spherocylindrical Particles (Figure 2)

Property		Small Scale	Large Scale
Bed height	h_{bed}	0.5 m	1.0 m
Bed width	w_{bed}	0.1 m	0.3 m
Bed depth	d_{bed}	0.015 m	0.05 m
Packed bed height	h_{pb}	0.1 m	0.3 m
Particle length	L_p	$6.0 \cdot 10^{-3}$ m	$12.0 \cdot 10^{-3}$ m
Rod length	L_{rod}	$4.5 \cdot 10^{-3}$ m	$9.0 \cdot 10^{-3}$ m
Particle diameter	d_p	$1.5 \cdot 10^{-3}$ m	$3.0 \cdot 10^{-3}$ m
Volume equivalent			
Spherical diameter	d_c	$2.6 \cdot 10^{-3}$ m	$5.3 \cdot 10^{-3}$ m
Bed weight	M_{bed}	0.11 kg	3.51 kg

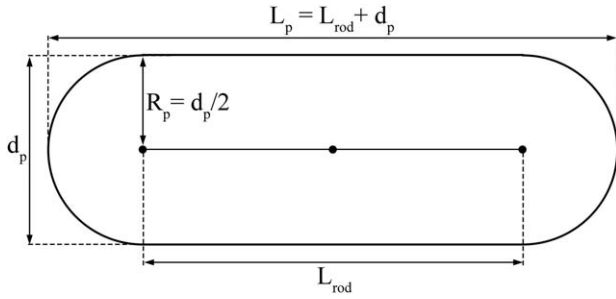


Figure 2. Geometry of the spherocylindrical particles. Dimensions are given in Table 1.

A Dantec Dynamics FlowSense EO 16M camera was used to capture images of the bed for DIA and PIV. Double frame images with a 2.0 ms interval were acquired at a rate of 3.0 Hz. Four LED lights arranged around the camera were used to illuminate the bed (Figure 1). These lights were set to illuminate the bed for 200 μ s for every frame taken.

Pressure drop

Pressure measurements are taken using the differential pressure sensor attached to the bottom of each bed (see Figure 1), at a frequency of 100 Hz. The pressure drop results are compared with correlations found in literature. These correlations are listed in Table 2. For comparison, measurements in the packed bed regime at increasing gas velocity will be used, which are not subject to channeling. The bed porosity is calculated from the measured bed height (Section) and weight of the bed.

Correlations 1–8 in Table 2 were developed for spherical particles. These can be applied to beds of nonspherical particles by replacing the particle diameter d_p with the surface volume equivalent diameter d_{SV} , (Eq. 1, where V_p and A_p are, respectively, the particle volume and surface area). The Ergun equation already takes into account the viscous and kinetic pressure losses. Multiple adaptations of the Ergun equation [22] take into account (Table 2, #2–8) wall effects by use of the hydraulic diameter D (Eq. 2). The correlation developed by Gibilaro³⁰ includes a correction term for beds with a high void fraction

Table 2. Correlations Used to Compare with the Acquired Pressure Drop Data

#	Expression(s)	Author	Conditions
1	$\frac{\Delta P}{L} = 150 \frac{(1-\epsilon)^2 \eta_g U_0}{\epsilon^3 d_p^2} + 1.75 \frac{1-\epsilon \rho_g U_0^2}{\epsilon^3 d_p}$	Ergun ²²	$D/d_p \gg 10$
2	$\frac{\Delta P}{L} = 150 \frac{(1-\epsilon)^2 \eta_g U_0}{\epsilon^3 d_p^2} M_{MH}^2 + 1.75 \frac{1-\epsilon \rho_g U_0^2}{\epsilon^3 d_p} M_{MH}$ $M_{MH} = 1 + \frac{4d_p}{6D(1-\epsilon)}$	Metha, Hawley ²³	$7 < D/d_p < 91$
3	$\frac{\Delta P}{L} = 130 \frac{(1-\epsilon)^2 \eta_g U_0}{\epsilon^3 d_p^2} + \frac{D/d_p}{2.28 + 0.335(D/d_p)} \frac{1-\epsilon \rho_g U_0^2}{\epsilon^3 d_p}$	Foumeny ²⁴	$3.23 < D/d_p < 23.8$
4	$\frac{\Delta P}{L} = K_1 \frac{(1-\epsilon)^2 \eta_g U_0}{\epsilon^3 d_p^2} M^2 + 1.75 \frac{1-\epsilon \rho_g U_0^2}{\epsilon^3 d_p} \frac{M}{B_W}$ $B_W = (k_1(d_p/D)^2 + k_2)^2$	Reichelt ²⁵	See Table 3
5	$\frac{\Delta P}{L} = 150 \frac{(1-\epsilon)^2 \eta_g U_0}{\epsilon^3 d_p^2} C_W^2 + 1.75 \frac{1-\epsilon \rho_g U_0^2}{\epsilon^3 d_p} C_{Wi}$ $C_W = 1 + \frac{\pi d_p}{6D(1-\epsilon)}$; $C_{Wi} = 1 - \frac{\pi^2 d_p}{24D} \left(1 - \frac{d_p}{2D}\right)$	Liu, Masliyah ²⁶	Unknown
6	$\frac{\Delta P}{L} = K_{1,Rai} \frac{(1-\epsilon)^2 \eta_g U_0}{\epsilon^3 d_p^2} + K_{2,Rai} \frac{1-\epsilon \rho_g U_0^2}{\epsilon^3 d_p}$ $K_{1,Rai} = 103 \left(\frac{\epsilon}{1-\epsilon}\right)^2 \left(6(1-\epsilon) + \frac{80d_p}{D}\right)$ $K_{2,Rai} = 2.8 \frac{\epsilon}{1-\epsilon} \left(1 - \frac{1.82d_p}{D}\right)^2$	Raichura et al. ²⁷	$5 < D/d_p < 50$
7	$\frac{\Delta P}{L} = 0.061 \frac{1-\epsilon}{\epsilon^3} \left(\frac{D}{d_p}\right)^{0.2} (1000\text{Re}_p^{-1} + 60\text{Re}_p^{-0.5} + 12) \frac{\rho_g U_0 d_p}{\eta_g}$ $\text{Re}_p = \frac{\rho_g U_0 d_p}{\eta_g}$	Montillet et al. ²⁸	$3.8 < D/d_p < 14.5$
8	$\frac{\Delta P}{L} = \left(185 + 17 \frac{\epsilon}{1-\epsilon} \left(\frac{D}{D-d_p}\right)^2\right) \frac{(1-\epsilon)^2 \eta_g U_0}{\epsilon^2 d_p^2} + \left(1.3 \left(\frac{1-\epsilon}{\epsilon}\right)^{1/3} + 0.03 \left(\frac{D}{D-d_p}\right)^2\right) \frac{1-\epsilon \rho_g U_0^2}{\epsilon^3 d_p}$	Cheng ²⁹	$1.1 < D/d_p < 50.5$
9	$\frac{\Delta P}{L} = \left(18 \frac{\eta_g}{\rho_g U_0 d_p} + 0.33\right) \frac{\rho_g U_0^2}{d_p} (1-\epsilon) \epsilon^{-4.8}$	Gibilaro ³⁰	$0.4 \leq \epsilon \leq 1$
10	$\frac{\Delta P}{L} = \frac{150 (1-\epsilon)^2 \eta_g U_0}{\phi^{3/2} \epsilon^2 d_p^2} + \frac{1.75 (1-\epsilon \rho_g U_0^2)}{\phi^{4/3} \epsilon^3 d_p}$	Nemec, Levec ³¹	$L_p/R_p \geq 1$
11	$\frac{\Delta P}{L} = \left(\frac{a}{\text{Re}_{Duct}} + \frac{b}{\text{Re}_{Duct}^c}\right) \frac{U_0^2}{2} \frac{\sum A_p}{4 \sum V_p} \frac{1-\epsilon}{\epsilon^3}$ $\text{Re}_{Duct} = \frac{4 \rho_g U_0 \sum V_p}{\eta_g (1-\epsilon) \sum A_p}$	Allen et al. ³²	See Table 3
12	$\frac{\Delta P}{L} = 4.466 \text{Re}_p^{-0.2} \phi^{0.696} \epsilon^{-2.945} e^{11.85(\log \phi)^2}$	Singh et al. ³³	$1000 < \text{Re} < 2700$

Table 3. Parameters for the Reichelt and Allen Equations

Parameters			Author	Particle Shape	Conditions
K_1	k_1	k_2			
150	1.5	0.88	Reichelt ²⁵	Spheres	$1.73 < D/d_p < 91$
154	1.15	0.87	Eisfeld, Schnitzlein ³⁴	Spheres	$1.624 < D/d_p < 250$
190	2.00	0.77	Eisfeld, Schnitzlein ³⁴	Cylinders	$1.624 < D/d_p < 250$
155	1.42	0.83	Eisfeld, Schnitzlein ³⁴	All	$1.624 < D/d_p < 250$
a	b	c			
240	10.8	0.1	Allen et al. ³²	Cubes	$Re > 700$
216	8.8	0.12	Allen et al. ³²	Cylinders	$Re > 700$
185	6.35	0.12	Allen et al. ³²	Rough spheres	$Re > 700$
150	3.25	0.15	Allen et al. ³²	Ellipsoids	$Re > 700$

$$d_{SV} = 6 \frac{V_p}{A_p} \quad (1)$$

$$D = \frac{2d_{bed} w_{bed}}{d_{bed} + w_{bed}} \quad (2)$$

Correlations 10–12 were developed specifically for nonspherical particles. They include the sphericity ϕ (Eq. 3) or incorporate the particle volume and area directly. Correlation 12 by Singh et al.³³ calls for the use of the volume equivalent diameter d_e (Eq. 4). Eisfeld and Schnitzlein³⁴ reported coefficients for correlation 4 by Reichelt²⁵ for nonspherical particles. These are given in Table 3, along with coefficients for correlation 11 by Allen et al.³²

$$\phi = \frac{\pi^{1/3}(6V_p)^{2/3}}{A_p} = \frac{d_{SV}}{d_e} \quad (3)$$

$$d_e = \left(\frac{6}{\pi} V_p\right)^{1/3} \quad (4)$$

Fourier analysis

A fast Fourier transform (FFT) of the pressure drop signals converts it to a frequency domain from its time domain. We

first apply a Hamming window function to the original pressure data to reduce spectral leakage. The squared amplitude of the resulting FFT is the power spectrum, which is routinely used to find dominant frequencies in the pressure signal. These dominant frequencies can give an indication of the bubble frequency and associated particle mixing in the fluidized bed. This analysis is crucial in cases where visual measurement techniques cannot be employed such as in 3D opaque systems often encountered in industry. For this purpose, pressure measurements are taken at 100 Hz for 10 min.

Digital Image Analysis

Bed height

In many studies, a threshold is applied to images to mark particle, bubble and freeboard areas.^{7,35,36} However, in this study a different approach is applied to the acquired images. To extract the bed height from images, the maximum intensity gradient along the height of the setup is found. This method allows for improved particle detection in cases where contrast between the particles and the backplate is low. The procedure used in this study is described in detail below.

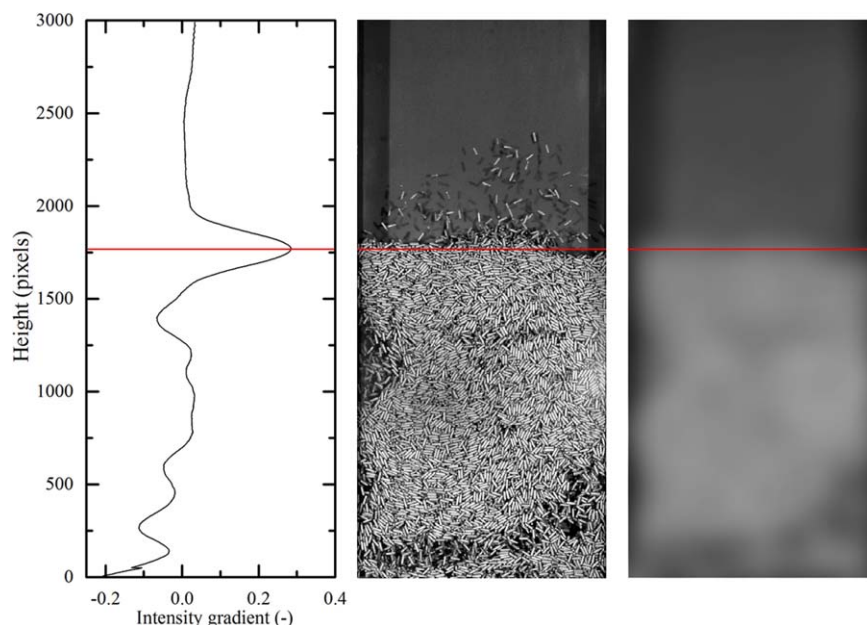


Figure 3. Demonstration of the bed height detection algorithm at $U_0=2.4\text{m/s}$.

Left: intensity gradient. Middle: original image. Right: filtered image. Red lines indicate the detected bed height. [Color figure can be viewed at wileyonlinelibrary.com]

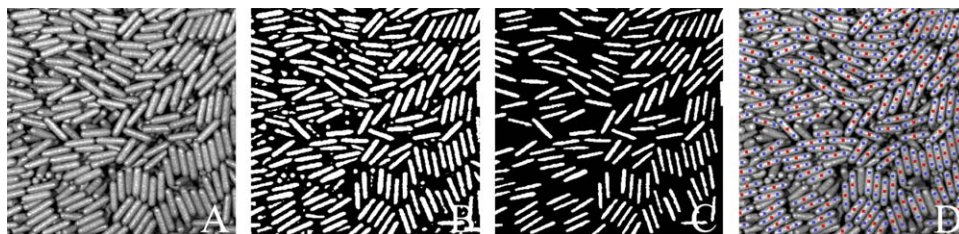


Figure 4. Example of the DIA procedure for orientation detection.

The image is cropped and its brightness and contrast are adjusted (A). Next, a threshold is applied to remove the background particles (B). All parts too small or large are removed (C). The center of mass of each particle is detected (D, red points). Last, the angle detection algorithm is applied (D, blue points). [Color figure can be viewed at wileyonlinelibrary.com]

All image analysis techniques reported in this study use MATLAB[®] and the Image Processing Toolbox[™]. The brightness and contrast of the cropped image are automatically adjusted to obtain a more homogeneous illumination. Next, the image is blurred using a Gaussian filter. The average intensity of each row of pixels is calculated, and this curve is further smoothed. Its derivative is approximated by linear interpolation between adjacent points. The bed height is then defined by the height of maximum gradient. The algorithm is demonstrated in Figure 3. To verify the accuracy of the algorithm, sampled results were manually inspected at all flow rates.

Particle orientation

For spherical particles, the particle orientation is of no concern, and particle positions can be detected using a circle detection method, such as the Hough transform.³⁷ Very elongated (needle-like) particles can be represented as lines on images and a Hough transform for detecting lines can be applied.³⁸ However, due to the intermediate aspect ratio of the particles used in this work, a different approach is needed. Hough transform methods for detecting ellipses have been developed, which can be used to detect the spherocylindrical

particles.³⁹ However, finding five parameters per particle (x -position, y -position, major axis diameter, minor axis diameter, and orientation), makes it very slow in processing the large images used in this study. Also correlation of all non-zero pixels in a five-dimensional space, makes it very memory consuming. For these reasons, a new method to detect particle orientation has been devised.

The procedure for detecting the particles and their orientation is described below. An example is shown in Figure 4. These steps ensure that only individual particles lying parallel to the front wall are selected.

1. The cropped image (Figure 4A) is imported and its brightness and contrast are adjusted.
2. An adaptive threshold is applied to separate the particles in the front plane from the surrounding shadows. (Figure 4B)
3. The edges are smoothed and parts either too small or too large are removed. (Figure 4C)
4. The particles are individually labelled and their center of mass is determined using the `regionprops` function in the MATLAB[®] Image Processing Toolbox[™]. (Figure 4D, red points)
5. The angle detection algorithm is applied. (Figure 4D, blue points) This algorithm is described below and is visualized in Figure 5.

- a. The aspect ratio of the particle is determined along two perpendicular axes. (Figure 5, top left)
- b. The axes are rotated and the aspect ratio is determined at each angle. (Figure 5, top right)
- c. The maximum aspect ratio is determined. The angle at which this occurs is taken as the particle angle. (Figure 5, bottom)

By manual inspection of images at all flow rates, it was estimated that approximately 90% of the particles oriented parallel to the front wall are detected by the algorithm. The efficiency of the angle detection is very high, >95% of the detected particles have their angle determined accurately. Multiple images at different flow rates were analyzed by hand and the results were compared with the algorithm results to confirm the detection accuracy. The efficiencies are equal for both beds because the entire setup and camera zoom is scaled with the particle size. The overall efficiency, the ratio of the particles with correct angles detected to the total number of particles in the bed is around 5%. While this may appear low, it is an intrinsic limitation of optical analysis of an opaque bed where only the particles closest to the transparent wall are visible, and is almost impossible to improve significantly.

Particle coalignment

To quantify the particle coalignment, a spatial autocorrelation function is used. This function describes the alignment of

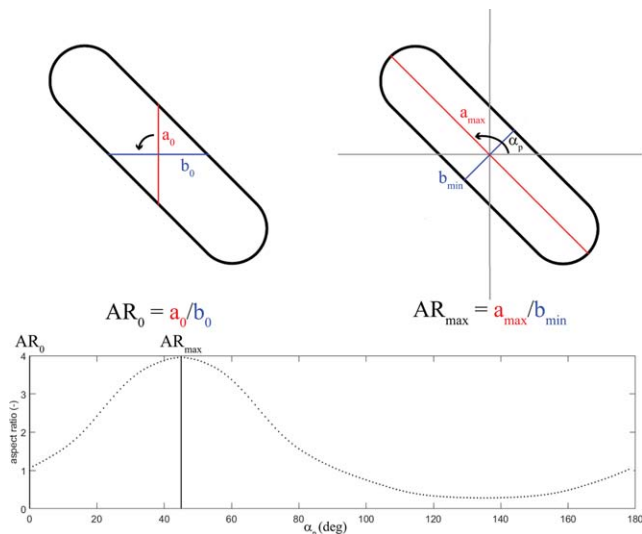


Figure 5. Algorithm for detection of particle orientation.

Top left: the length and width of the particle are evaluated along two perpendicular axes. Top right: the axes are rotated around the center of the particle. Bottom: the angle α_p that the rotating axis makes with the positive x -axis for maximum aspect ratio is extracted. [Color figure can be viewed at wileyonlinelibrary.com]

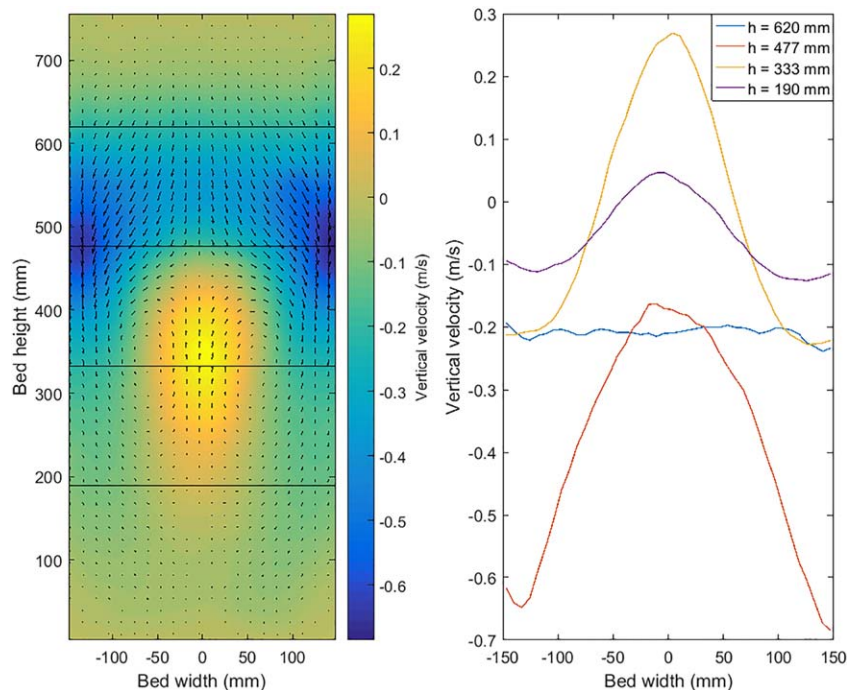


Figure 6. Left: measured average velocity profile at $U_0=1.6U_{mf}$, using 5000 double-frame images.

Vectors represent velocity magnitude and direction, colors represent vertical velocity magnitude. Right: Vertical velocity magnitude at different heights in the bed. [Color figure can be viewed at wileyonlinelibrary.com]

a certain particle with another particle, separated by a distance r . The function definition is derived from the scalar product of the unit orientation vectors associated with each particle, and accounts for the symmetry of the particles. The autocorrelation function is defined by Eq. 5, where $C(r)$ denotes the correlation value at separation r , and $\alpha(r)$ signifies the in-plane orientation angle of a particle located distance r from the origin. Normalization is done assuming the particle orientation is noncorrelated at infinite separation, that is, $\langle \cos^2(\alpha(0) - \alpha(\infty)) \rangle = 1/2$

$$C(r) = \frac{\langle \cos^2(\alpha(0) - \alpha(r)) \rangle - \langle \cos^2(\alpha(0) - \alpha(\infty)) \rangle}{\langle \cos^2(\alpha(0) - \alpha(0)) \rangle - \langle \cos^2(\alpha(0) - \alpha(\infty)) \rangle} \quad (5)$$

$$= 2\langle \cos^2(\alpha(0) - \alpha(r)) \rangle - 1$$

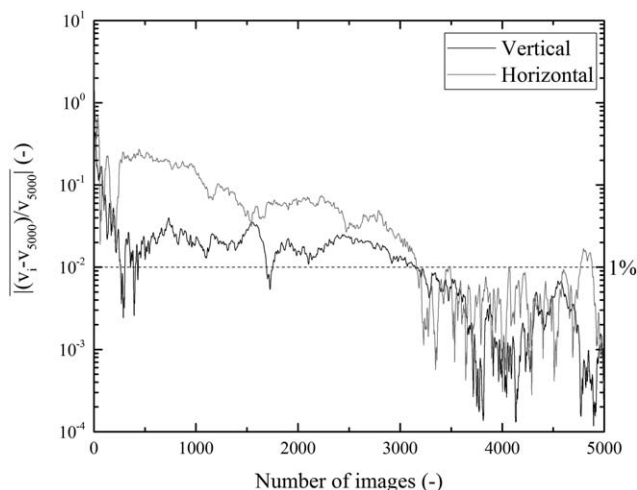


Figure 7. Relative deviation from mean velocity as a function of number of images taken. v_i represents the mean velocity calculated from i images.

To extract the correlation curve from experimental data, r is discretized into bins, up to the cutoff radius r_{cut} (set to five particle lengths). For each pair of particles with a separation smaller than r_{cut} , the correlation value is calculated and added to the mean in the associated bin.

The analysis is performed for the entire height of the large bed. The bed is divided into three regions: $< 2L_p$ from the side wall, $2L_p - 6L_p$ from the side wall and $> 6L_p$ from the side wall. The correlation curves are calculated separately for each region. These boundaries are chosen such that the effect from the side walls can be assessed, while maintaining enough data in each region to obtain smooth curves.

Particle image velocimetry

PIV analysis was performed using LaVision DaVis 8.2.3 software. The multipass method was selected, using one pass with a 256×256 pixels interrogation cell and 50% overlap, followed by three passes with a 128×128 pixels interrogation cell and 75% overlap. As the maximum particle displacement between two frames is estimated at approximately 20 pixels, it is unlikely a particle will cross interrogation cell boundaries. Tests show that 3500 double-frame images are sufficient to calculate time-averaged velocity profiles. See Figures 6 and 7. At first glance, the averaged velocity profiles in Figure 6 may seem unphysical. However, this is a result of different time scales of the particles moving up and down. The particles move down over larger time scales (at higher average void fraction) than the particles moving up. Therefore, when cell-based velocities are averaged over a number of frames, without taking into account the actual void fraction, we find a net downward velocity. See PTV results Figure 26.

Void fraction calculation

To convert the velocity data obtained from PIV measurements to the mass flux, the local void fraction in the bed must

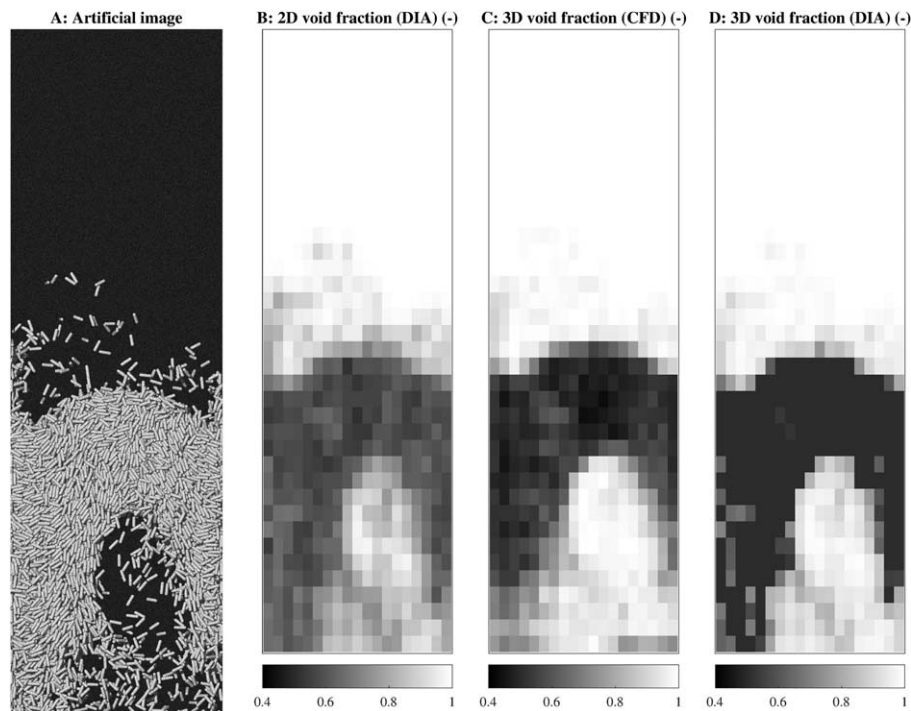


Figure 8. Demonstration of the void fraction calculation from artificial images.

The artificial image (A) is generated to resemble experimental conditions as closely as possible. Using the image analysis algorithm, the 2D void fraction (B) is calculated, which is compared with the 3D void fraction from the CFD model (C). From this, the coefficients in Eq. 7 are fitted, resulting in the 3D void fraction from image analysis (D).

be known. This is expressed by Eq. 6, where $\vec{\phi}_m$ is the local mass flux, \vec{v} the particle velocity, ρ_p the particle density, and ϵ the local void fraction

$$\langle \vec{\phi}_m \rangle = \langle \vec{v} \rho_p (1 - \epsilon) \rangle \quad (6)$$

First, the two-dimensional void fraction is obtained. Two commonly used approaches to obtain the 2D void fraction are to distinguish between the bubble phase and emulsion phase in the bed^{35,40} or to correlate the average pixel intensity in an area with the local void fraction in that area.^{16,41} However, both of these methods prove to have their own limitations. The fluidization behavior of the Geldart D particles used in this study does not allow for formation of discrete distinguishable bubbles. Thus, the first method cannot be applied here. The latter method produces unsatisfactory results due to the low contrast between particles and background and the nonuniform lighting. Therefore, the latter method has been extended with a threshold-step, as described below.

1. The particles are separated from the background as reported in Section (Steps 1–2).

2. The image is divided into grid cells of identical size as the PIV results.

3. The total area of the particle phase in each grid cell is calculated.

4. Particle pixel area is converted linearly to 2D solid volume fraction by use of the known total solid volume in the bed.

Next, the 2D void fraction is converted to the physical 3D void fraction. This is done using the method described by De Jong et al.⁸ and Van Buijtenen et al.,⁴¹ which is expressed by Eq. 7. Here, B gives the location of the asymptote and A scales the curve. Because the 3D void fraction is a property not easily measured experimentally, CFD-DEM simulation data is used

to find fitting parameters A and B . The simulation data is used to create artificial images of the small setup using OVITO[®] software.⁴² The lighting is adjusted to represent experimental conditions as closely as possible. The algorithm above is then used to obtain the 2D void fraction from these images, which can be compared to the physical 3D void fraction from the simulation results. A demonstration of this method is given in Figure 8

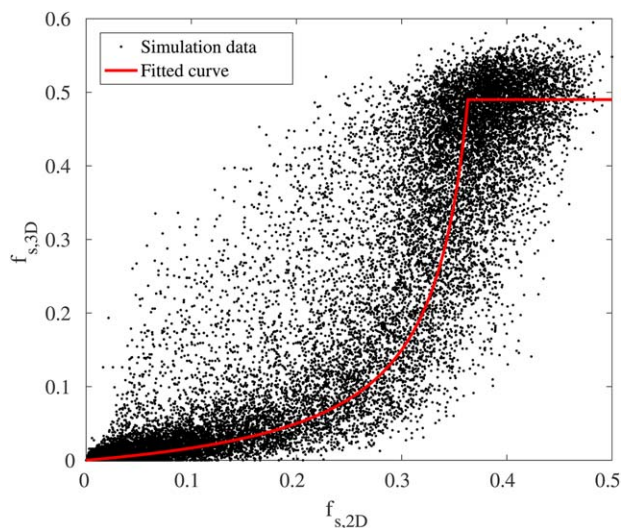


Figure 9. Correlation of 2D and 3D solid volume fraction.

Points represent the simulation data, the line represents the fitted curve (Eq. 7). Parameters found are $A = 0.05$ and $B = 0.45$. [Color figure can be viewed at wileyonlinelibrary.com]

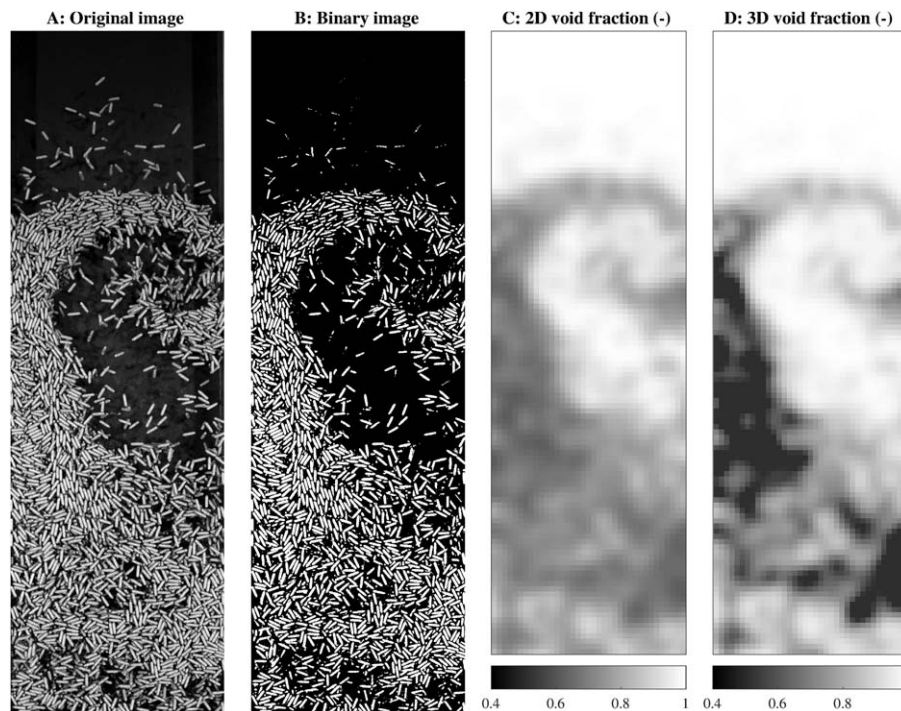


Figure 10. Demonstration of the void fraction calculation on the small bed.

The original image (A) is binarized (B). From the particle phase area, the 2D void fraction (C) is calculated, which is then converted to the 3D void fraction (D) according to Eq. 7.

$$f_{s,3D} = \begin{cases} f_{s,3D,\max} & \text{for } f_{s,3D} \geq f_{s,3D,\max} \\ \frac{A_f f_{s,2D}}{B_f - f_{s,2D}} & \text{for } f_{s,3D} < f_{s,3D,\max} \end{cases} \quad (7)$$

Nonlinear curve fitting was used to obtain the values for A_f and B_f . The results from this fitting is shown in Figure 9. These were obtained using 190 artificial images from a simulation of the small bed at $U_0 = 2.6$ m/s. From the known packed bed height, it is found that $f_{s,3D,\max} = 0.49$. The parameters found are $A_f = 0.05$ and $B_f = 0.45$. The value of A_f is adapted slightly for each image to ensure mass conservation. A demonstration of the algorithm is given in Figure 10.

Particle tracking velocimetry

To investigate the movement and orientation of individual particles, PTV was used. In PTV the displacement of each individual particle is tracked, as opposed to PIV, where the average displacement of groups of particles is measured. For these measurements, a LaVision HighSpeedStar camera was used to capture a 15×15 cm area of the large bed. A frame rate of 500 Hz and a resolution of 1024×1024 pixels were used. This framerate was chosen such that the particle movement can be tracked accurately. To track the particles over multiple frames, a Nearest Neighbor Search interrogation strategy⁴³ was used. This algorithm is explained below. An example is shown in Figure 11.

1. The position and orientation of the particles in the frame are analyzed using the algorithm described in Section.

2. The distance between each particle in the current frame and each particle in the previous frame is calculated.

3. Pairs of particles with minimal displacement are given the same index.

4. Any possible conflicts where one particle is linked to multiple other particles due to a particle moving in or out of the frame are eliminated by selecting the pair with the smallest displacement.

5. Any particle in the current frame that is not linked to a particle in the previous frame is given a new index.

6. Steps 1–5 are repeated for all frames.

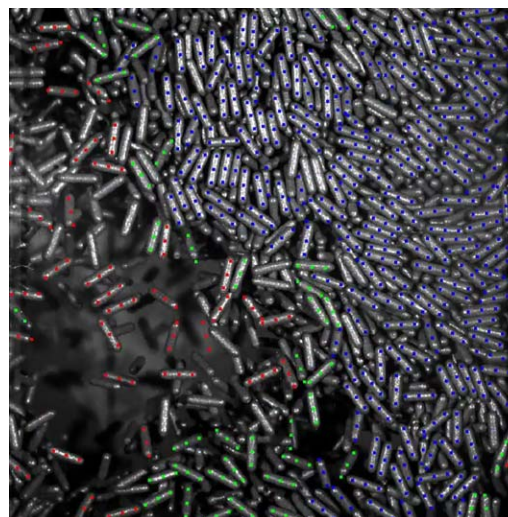


Figure 11. An example of PTV procedure showing coordination number indicated by color codes: blue (dense) with CN 9 or higher, green (medium) with CN from 5 to 8, red (dilute) having CN less than 5.

[Color figure can be viewed at wileyonlinelibrary.com]

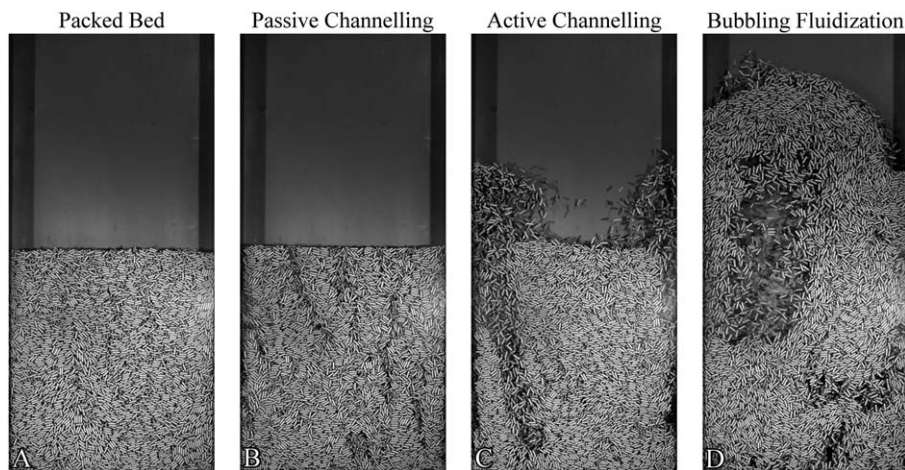


Figure 12. Examples of the different fluidization regimes observed in the large bed with increasing gas velocity.

A: $U_0 = 0$ m/s, B: $U_0 = 1.5$ m/s, C: $U_0 = 1.9$ m/s, D: $U_0 = 2.4$ m/s.

7. Paths shorter than 4 frames are removed from the data, as they are not suitable for analysis.

8. Using the camera resolution and frame rate, velocities are calculated from their displacement.

9. Based on its number of nearest neighbors, the coordination number (CN), defined as the number of neighbors within a radius of L_p , is calculated for each particle.

10. To account for walls, the CN is normalized using the area of the search area which lies inside the bed.

orientation, particle co-ordination number and particle co-alignment are presented for the large particles.

Fluidization regimes

Over the range of gas velocities, the different fluidization regimes described below are observed. Examples of each regime are shown in Figure 12. Similar behavior was observed by Kruggel-Emden and Vollmar⁴⁴ for elongated cuboids of comparable dimensions as the large particles.

- Packed Bed (PB): At low flow rates, the particles are stationary. The gas passes through the voids between the particles without moving the bed. (Figure 12A)
- Passive Channelling (PC): The gas flow creates paths free of particles. These channels are fairly stable and exist for

Results and Discussion

In this section, results obtained from the aforementioned experimental techniques are presented. The results for particle

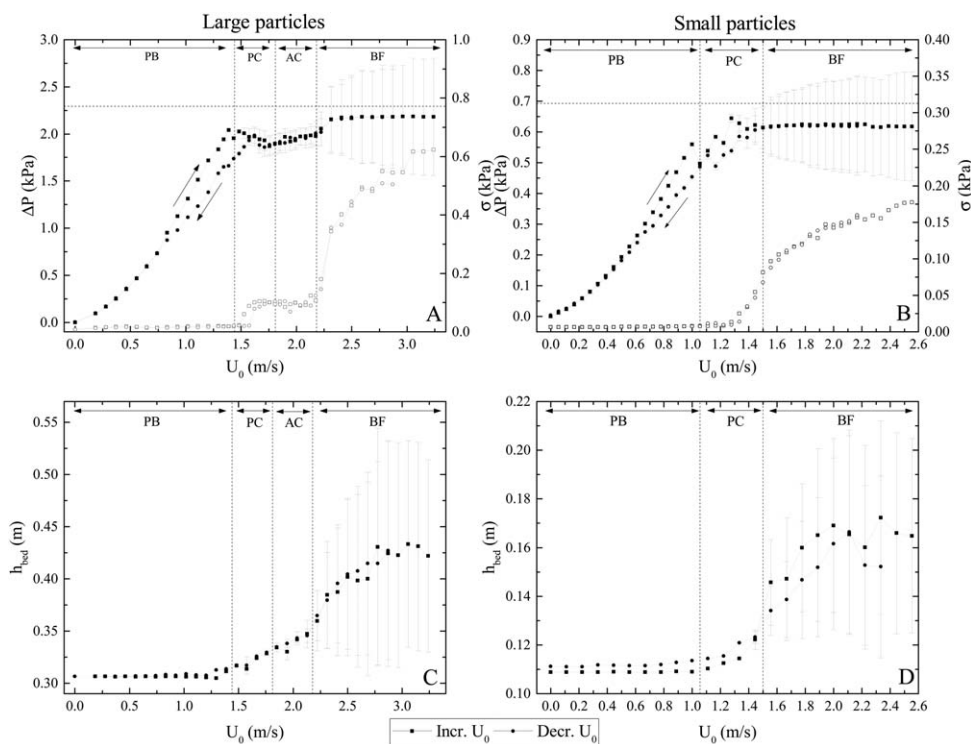


Figure 13. Measured pressure drop (A–B) and bed height (C–D) for the large (A–C) and small (B–D) particles.

The open symbols represent standard deviation in pressure drop. Vertical dashed lines show the transition between fluidization regimes. Horizontal dashed lines show the static pressure drop (Eq. 9).

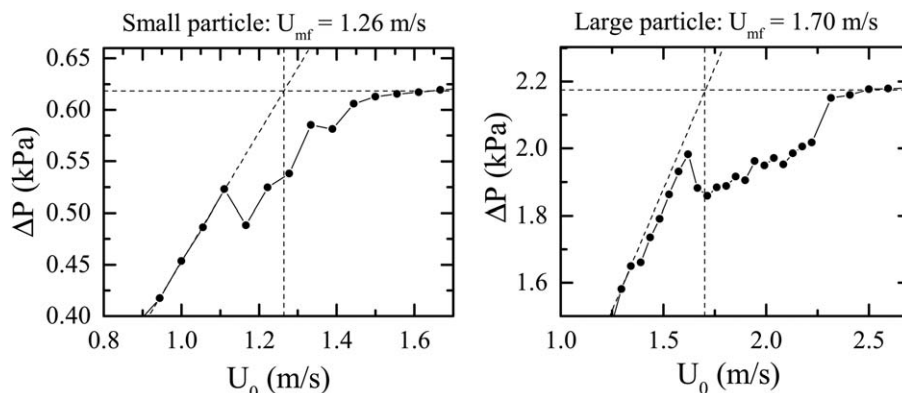


Figure 14. Determination of the minimum fluidization velocity (U_{mf}).

multiple minutes. When the gas velocity is lowered back into the packed bed region, the channels remain. (Figure 12B)

- Active Channeling (AC): Large amounts of particles are sucked into the channels and fountains are formed. The channels are wider compared to the passive channeling phase. They collapse rapidly and new paths are created continuously. As particles move up through the channels, there is a slow downward movement in the bulk phase. When the flow rate is increased, bubbles start moving through the channels. This regime is only observed for the large particles. One of the possible reasons for this is particle roughness which is relatively more pronounced for smaller particles. The smaller particles therefore need additional force to be pulled from a relatively dense packing. (Figure 12C)

- Bubbling Fluidization (BF): Bubbles form close to the distributor plate, which coalesce and move upward. When bubbles erupt at the surface, particles are thrown high into the freeboard region. At higher gas velocities, bubbles grow larger. In this state, the bed is very chaotic and unstable. Particles show interlocking behavior, where they move in large packed groups. (Figure 12D) In general, it is observed that normal bubbling patterns, as observed for spherical particles, are suppressed for non-spherical particles. The formation and relatively smooth passage of bubbles is inhibited due to particle entanglement, which leads to large internal

particle stresses and difficulties for particles to move relative to each other.

A possible correlation can be observed between regimes observed for elongated particles and spherical particles with a high coefficient of friction or cohesive forces. Elongated particles are prone to channeling, similar to fluidization behavior observed for Geldart C particles.⁴⁵ In both cases, the particles under consideration have to overcome the resistance of surrounding relatively dense packing of particles to be able to move. Once the particles overcome this critical force with the help of fluid drag, the steady structure breaks. The surrounding particles are dragged with the fluid and follow the created flow path, which we term channeling. Thus, even though the physical origin for the observed channeling behavior is different, entanglement versus cohesive forces, the effect is very similar.

Pressure drop

Results for the pressure drop measurements are shown in Figures 13A, B. Measurements were taken for 100 s at 100 Hz at both increasing and decreasing flow rate. Error bars indicate the standard deviation of the measurement, defined by Eq. 8, where S is the standard deviation and A is a series of N measurements, of which \bar{A} is the mean value. The minimum

Table 4. Coefficient of Determination for the Pressure Drop Correlations

#	Author	R^2
1	Ergun	0.97
2	Metha & Hawley	0.96
3	Foumeny	0.81
4-1	Reichelt	0.88
4-2	Eisfeld & Schnitzlein (spheres)	0.90
4-3	Eisfeld & Schnitzlein (cylinders)	0.97
4-4	Eisfeld & Schnitzlein (all shapes)	0.95
5	Liu & Masliyah	0.97
6	Raichura et al.	0.38
7	Montillet et al.	0.98
8	Cheng	0.74
9	Gibilaro	0.93
10	Nemec & Levec	0.48
11-1	Allen et al. (cubes)	<0
11-2	Allen et al. (cylinders)	<0
11-3	Allen et al. (rough spheres)	0.62
11-4	Allen et al. (ellipsoids)	0.61
12	Singh et al.	<0

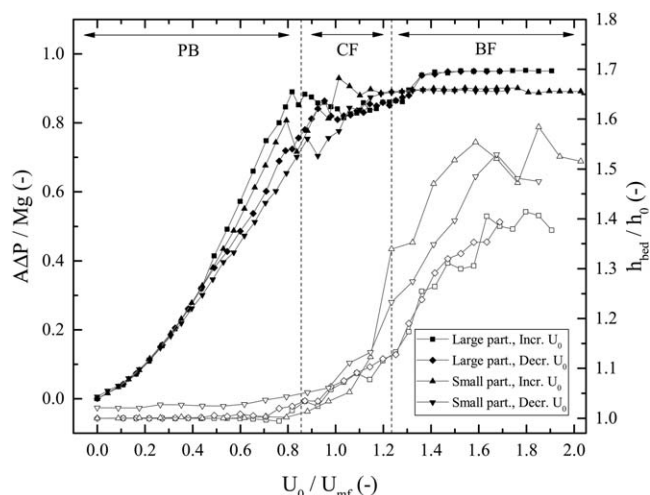


Figure 15. Normalized pressure drop and bed expansion as a function of normalized gas velocity for both particle sizes.

Solid symbols represent pressure drop, open symbols show the bed expansion.

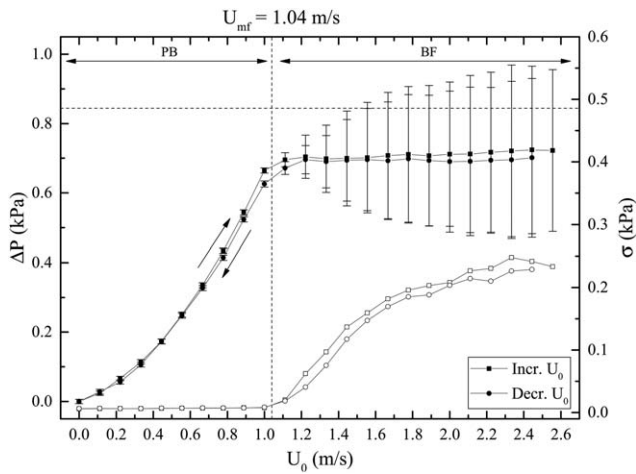


Figure 16. Pressure drop over the small setup filled with spherical particles.

Particles are of equal volume as the small spherocylinders. Open symbols indicate standard deviation of the pressure fluctuations. The horizontal dashed line represents total weight of the particles.

fluidization velocity (U_{mf}) was determined by the intersection of the static pressure drop and the packed bed pressure drop at decreasing flow rate, according to Kunii and Levenspiel.⁴⁶ This procedure is shown in Figure 14. Values of $U_{mf} = 1.26$ m/s (small particle) and $U_{mf} = 1.70$ m/s (large particle) were found

$$S = \sqrt{\frac{1}{N-1} \sum_{i=1}^N |A_i - \bar{A}|^2} \quad (8)$$

The pressure drop curves show a plateau at a value lower than the static pressure drop, indicating channeling.⁴⁷ In the channeling regimes, the pressure drop levels off, and pressure fluctuations start to occur. In the bubbling region, pressure drop increases and reaches a constant value (static pressure drop). There are very large pressure drop fluctuations, caused

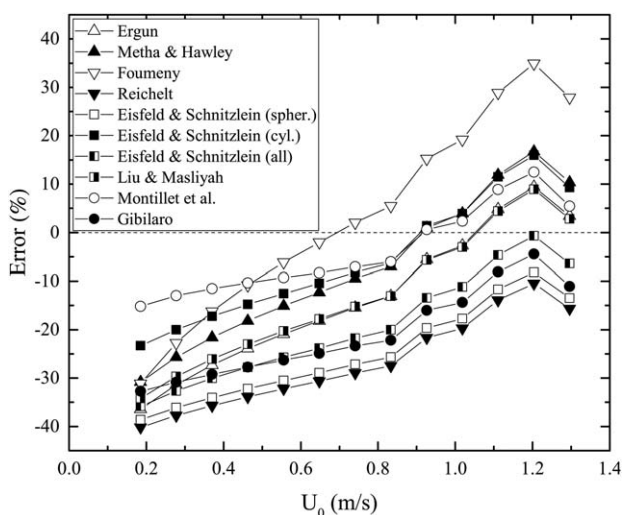


Figure 17. Relative error of all pressure drop correlations with $R^2 > 0.8$, as a function of superficial gas velocity.

(a) Elongated particles. (b) Spherical particles.

by the large bubbles in the system⁴⁸ The difference between the increasing and decreasing flow rate curves show that when gas velocity is lowered from the PC to PB regime, the channels remain, as indicated by the lower pressure drop.

The pressure drop caused by the weight of the bed is expressed by Eq. 9. This value is 5–10% higher than the measured static pressure drop. This indicates part of the particle weight is supported by the bed walls and bottom plate. As the small setup is smaller relative to the particle size than the large bed, the difference is larger (Figure 13)

$$\Delta P = \frac{g M_{bed}}{A} \quad (9)$$

Spherical particles

To compare the fluidization behavior of the spherocylinders with that of spheres, the pressure drop over the small setup filled with approx. 9500 spherical particles was measured. These particles were fabricated from the same Alumide material and are of equal volume as the small spherocylinders ($d_p = 2.6 \cdot 10^{-3}$ m). Results are shown in Figure 16. For these particles no channeling is observed; at the minimum fluidization velocity of 1.04 m/s the bed immediately transfers from the packed bed to bubbling fluidization regime. This proves that the observed fluidization behavior is caused by the particle shape, not by their material or size. When Figure 16 is compared to Figure 13, we find that the minimum fluidization velocity for spherical particles is lower compared to

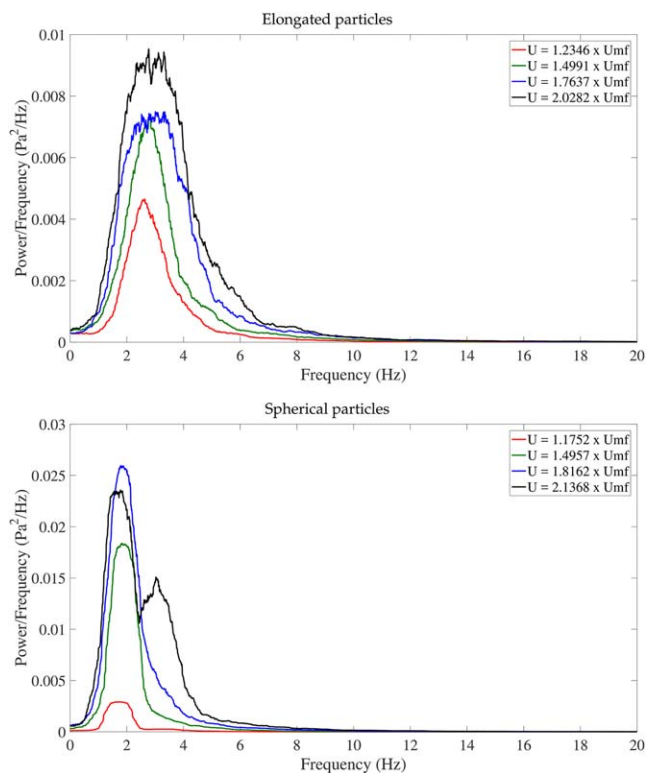


Figure 18. Power spectrum of pressure drop for small spherocylinder particles (top) and volume equivalent spherical particles (bottom) at different gas inlet velocities (U) shown as a function of minimum fluidization velocity (U_{mf}).

The curves are smoothed for clear representation. [Color figure can be viewed at wileyonlinelibrary.com]

nonspherical particles (of equivalent volume). This is due to the fact that when the flow rate is lowered, nonspherical particles are prone to form channels. As the gas flow rate is further lowered, these channels remain to exist, therefore allowing a significant amount of gas to pass through. This leads to a higher U_{mf} compared to spherical particles.

Pressure drop correlations

The predictive quality of a correlation is expressed by its coefficient of determination, noted R^2 (Eq. 10, where y are the measured values for the nonspherical particles and f the predicted values). Table 4 shows the R^2 for all correlations given in Table 2, when used to predict pressure drop over the large particle bed. It can be seen that the correlation of Montillet et al. (7) most accurately predicts the pressure drop in the packed bed regime, while the correlations by Ergun (1), Liu and Masliyah (5), and Einfeld and Schnitzlein (4–3) perform satisfactory as well. Figure 17 shows the relative error (Eq. 11) of all correlations with $R^2 > 0.8$ as a function of the gas velocity. Most correlations underestimate the pressure drop at low flow rates, and overestimate at higher flow rates. It is to be noted that the correlations have been developed for specific particle and setup specifications. For example, the correlation of Reichelt and Allensee in Table 3 is developed specific to spheres, cylinders, cubes, and so forth. On the same hand, we use these correlations to measure pressure drop for a bed of spherocylindrical particles. Therefore, some correlations perform better than others. It can also be seen that the error shows a positive trend with increasing gas velocity. At low velocity, all correlations under predict the pressure drop more than at higher velocity. At zero gas velocity, particles align with each other, forming very small spaces between them and increasing the pressure drop. Approaching the minimum fluidization velocity, particles slowly start aligning with the gas flow and form channels between them. This lowers the overall pressure drop. As the pressure drop correlations do not take these changing orientation effects into account, they under predict at low gas velocity and over predict at the higher gas velocities

$$R^2 \equiv 1 - \frac{\sum (y_i - f_i)^2}{\sum (y_i - \bar{y})^2} \quad (10)$$

$$\text{Error} = \frac{\Delta P_{\text{pred}} - \Delta P_{\text{meas}}}{\Delta P_{\text{meas}}} \cdot 100\% \quad (11)$$

Pressure drop Fourier analysis

Figure 18 shows the FFT analysis of pressure drop for small particles and their volume equivalent spherical particles. The curves are smoothed using moving window averaging. It can be seen that the dominant frequency is around 3 Hz and slightly increasing with increasing gas velocity. This was also confirmed from visual observations of the bubble frequency in the bed. It can also be seen that the peaks are sharper for spherical particles and broader for elongated particles. This indicates a clear preference towards bubble formation for spherical particles and more chaotic behavior of nonspherical particles. Rod-like particles oppose the formation of bubbles. At high gas flow rates, for spherical particles we observed that bubbles erupt with varying intensity. Once a large intensity bubble has passed, a large volume of gas leaves the bed leading to small intensity bubbles. This is the reason we observe double peaks at higher gas flowrates for spherical particles.

Bed height

Figures 13C, D shows the measured bed height. The regimes shown in Figure 12 are also reflected in bed height measurements. From the onset of channeling, the bed slowly expands. In the bubbling fluidization regime, the bed height increases rapidly. It is also clear that at this high flow rate, the fluctuations in bed height become very strong. As the particles are in the Geldart D class, fluidization is very unstable.⁴⁹ There is no sharp, identifiable bed height. Instead, particles are thrown high into the freeboard region and form large bubbles, as shown in Figure 12D.

Figure 15 shows the normalized pressure drop and bed height as a function of normalized gas velocity for both large and small particles. It is clear from the plot that the behavior of the particles is similar for both the particle sizes. This indicates that the particle behavior is shape induced.

Void fraction and mass flux

Figure 19 shows the velocity and mass flux profiles for the large bed at $U_0 = 3.24$ m/s. As can be seen, at a bed height of 600 mm the average particle velocity shows a net downward flow. However, when accounted for void fraction, the average mass flux profile shows net mass flux close to zero at different heights of the bed. In Figure 20, mass flux profiles obtained from PIV in both the small and large setup are shown. These profiles show the transition from channeling to the vigorously bubbling fluidization state. At gas velocities just above the minimum fluidization velocity, solids circulation is dominated by channeling and particle raining. As the gas velocity progresses in the bubbling fluidization regime, the well-known circulation pattern emerges, where particles mainly move up through the center and come down along the walls. This shows that, while their nonsphericity delays the fluidization of the spherocylindrical particles, at sufficiently high gas velocities solids circulation is qualitatively similar to that of beds of spherical particles. Figure 21 shows a quantitative comparison of vertical mass flux for the small and large bed at one height.

As the particles are circulating in a closed system, there should be zero net mass flux through each horizontal plane in the bed. However, from the obtained velocity profiles combined with solid volume fraction calculation via DIA, current results do not entirely follow this behavior, especially for the large setup. This is caused by the inaccuracy of the void fraction calculation; as the frontal area of the bed is very large, it is very challenging to obtain a uniform lighting. This results in discrepancies in the local void fraction, which reflect in the mass flux profile. As for the small bed it is much more straightforward to obtain a uniform lighting, the mass flux results are much more accurate. The discrepancy in mass flux can partly be also due to the comparatively large bed depth while the optical techniques we employ limit measurements to the frontal portion of the bed.

Particle orientation

Figure 22 (top) shows the Probability Density Function (PDF) for the particle orientation in the large setup at different flow rates. The PDF is given by Eq. 12, where $N_p(\alpha)$ is the number of particles at angle α

$$\text{PDF}(\alpha) = \frac{N_p(\alpha)}{\int_{-90}^{90} N_p(\alpha) d\alpha} \quad (12)$$

From zero flow rate up to the onset of bubbling fluidization, particles predominately lie down horizontally, as is expected

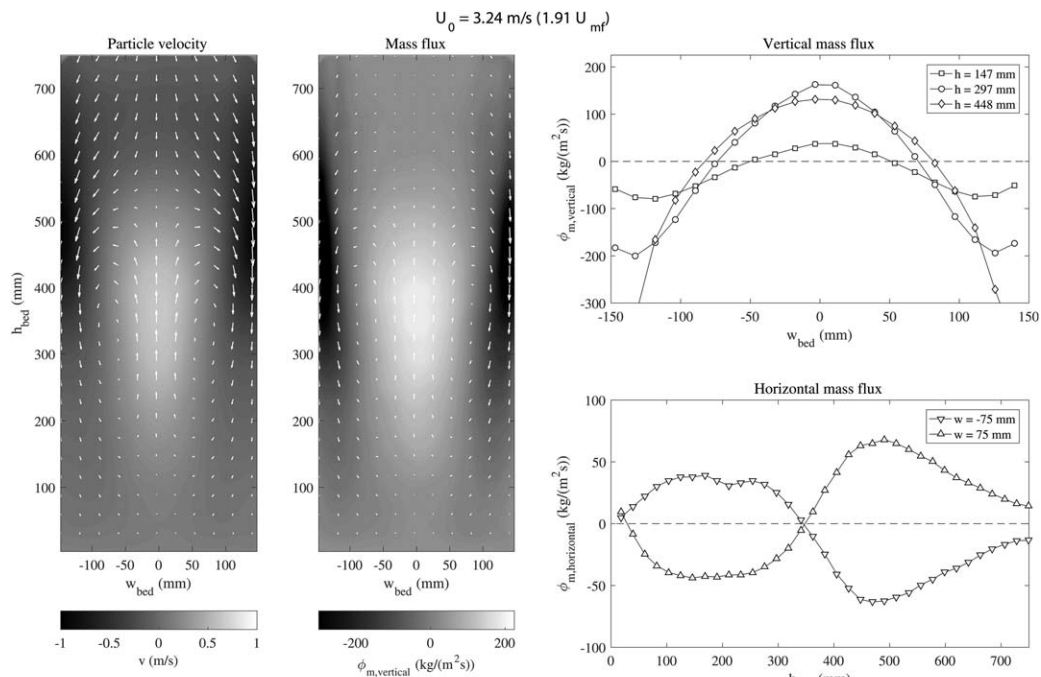


Figure 19. Particle velocity and mass flux results from experiments in the large setup at $U_0 = 3.24$ m/s.

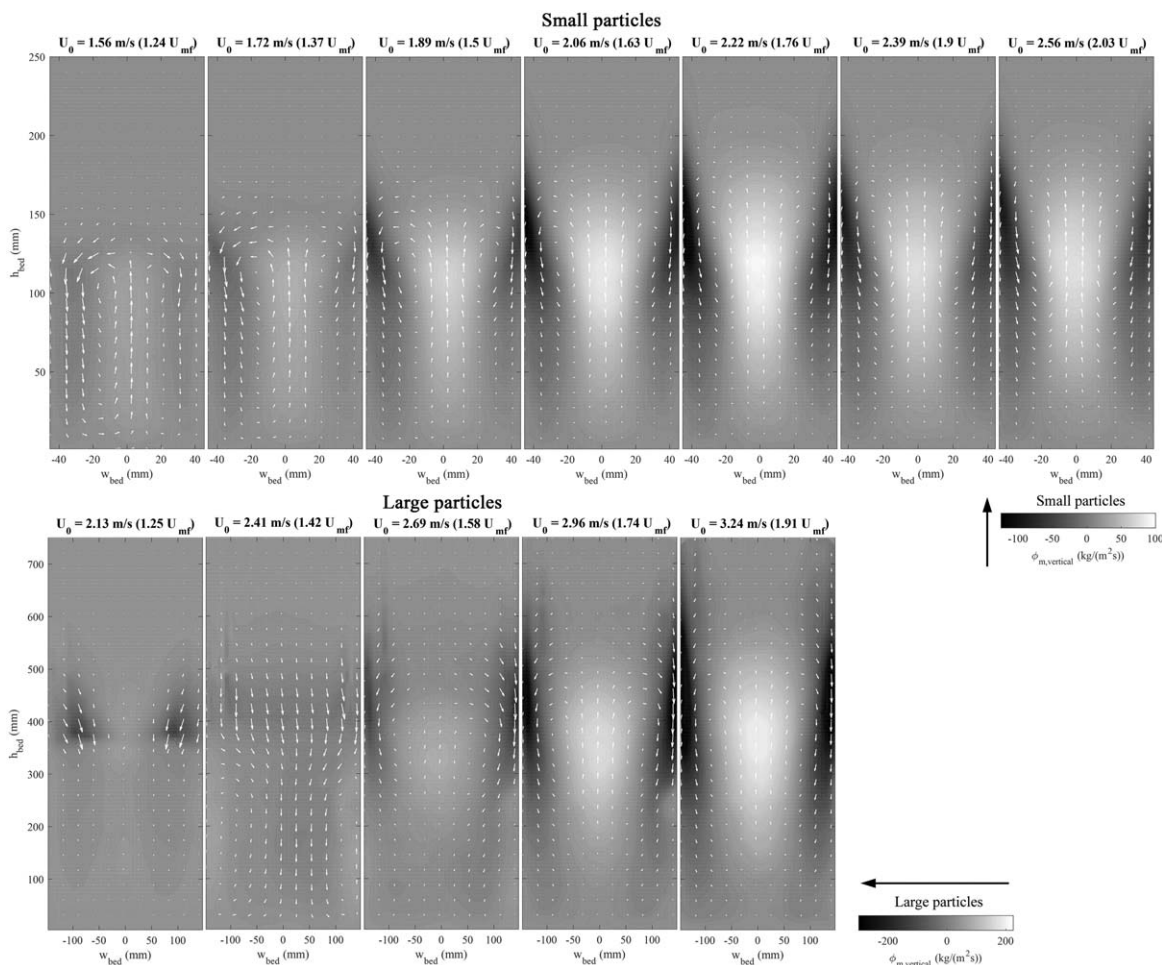


Figure 20. Mass flux profiles at different flow rates for the small (top) and large (bottom) particles.

Arrows represent mass flux magnitude and direction. Background color represent vertical massflux magnitude, indicated by the color bars. Note that the vector length scale is not consistent between figures.

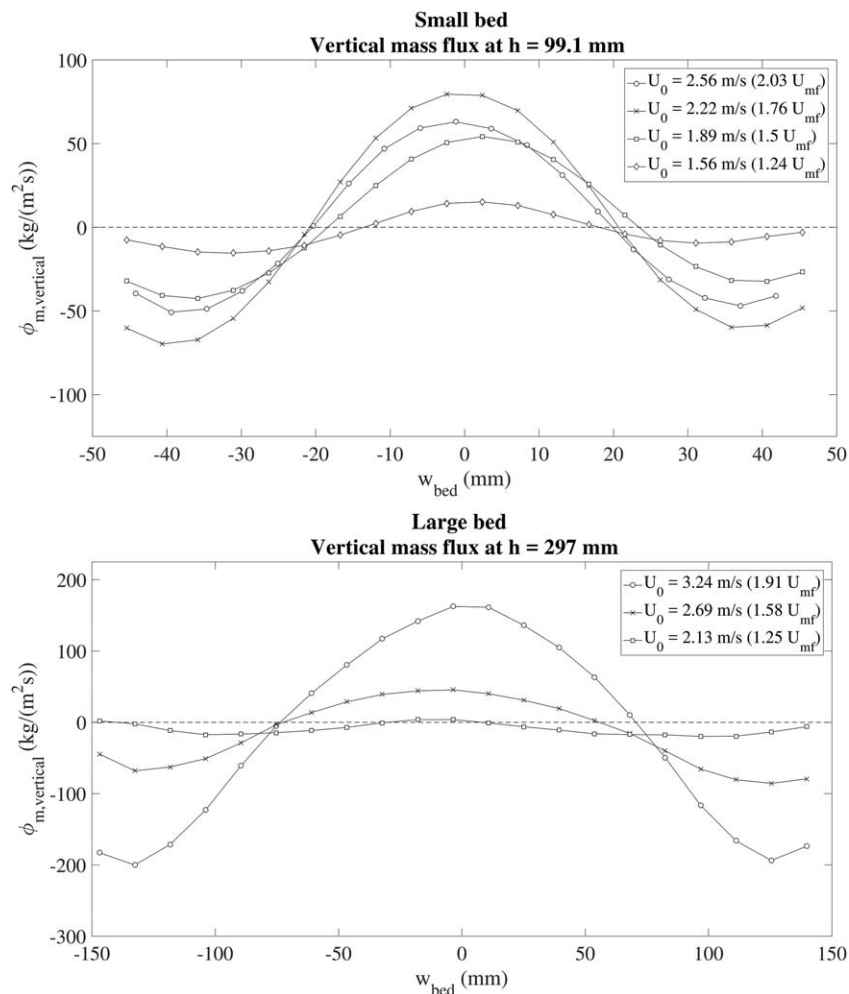


Figure 21. Mass flux profiles at different flow rates for the small bed (top) at height 99.1 mm and large bed (bottom) at height 297 mm.

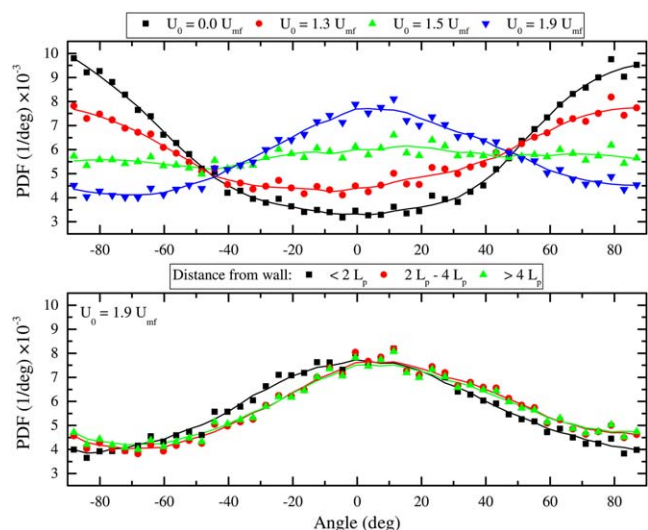


Figure 22. Top: PDF of the particle orientation at different flow rates.

An angle of 0 degrees corresponds with upright particles. Bottom: orientation PDF at the highest flow rate ($U_0=1.9U_{mf}$) separated for different locations in the bed. Lines are smooth fits. [Color figure can be viewed at wileyonlinelibrary.com]

from a particle at rest. At high gas velocity, the flow causes particles to align themselves vertically. As the particles are pushed up at high gas velocities, the interaction with surrounding particles causes them to align themselves vertically. At intermediate flow rates, there is no clear preferred orientation. Overall, preferred orientational behavior cannot be attributed to one single factor but is a result of several competing factors including particle–particle interaction, hydrodynamic lift, torque, and drag. From Figure 22 (bottom), which shows the PDF at the highest flow rate at different positions in the bed, it can be seen that the upright position of the particles is due to the gas flow, not due to wall proximity. Particles close to the wall and in the bulk show a very similar PDF.

Particle coalignment

Figure 23 shows a snapshot of the large bed at $U_0=2.13$ m/s. The particles are largely coaligned within a distance of approximately one particle length from each respective particle. These visual observations of coalignment below a particle length reflects in our quantitative measurements. Results of the orientation autocorrelation in the large bed at $U_0=2.13$ m/s are shown in Figure 24. The solid lines and symbols represent the measured data, the dashed lines show the fitted exponential decay. At correlation lengths below the particle length,

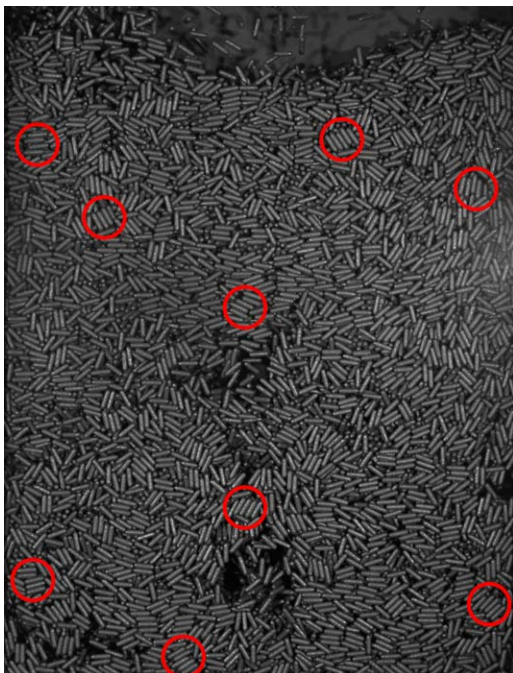


Figure 23. An example of particle coalignment for the large bed at $U_0=2.13$ m/s.

The red circles indicate a few instances of particles largely coaligned within a distance of one particle length from a respective particle. [Color figure can be viewed at wileyonlinelibrary.com]

there is direct orientational particle–particle interaction (due to particles in contact with each other). This results in a high correlation value, which decays fast. At larger correlations length, there is indirect orientational interaction between the particles, leading to an (approximately) exponentially decaying correlation value. By fitting Eq. 13 to the correlation curves, a correlation length λ can be found. The pre-exponential factor a_{pre} represents the strength of direct orientational interaction relative to the indirect orientational interaction

$$C(r)|_{r>L_p} = a_{pre} \exp\left(-\frac{r}{\lambda}\right) \quad (13)$$

A value of $a_{pre} = 1$ represents zero direct orientational interaction, as is expected for nearly spherical particles. A value of $a_{pre} = 0$ represents zero indirect orientational interaction,

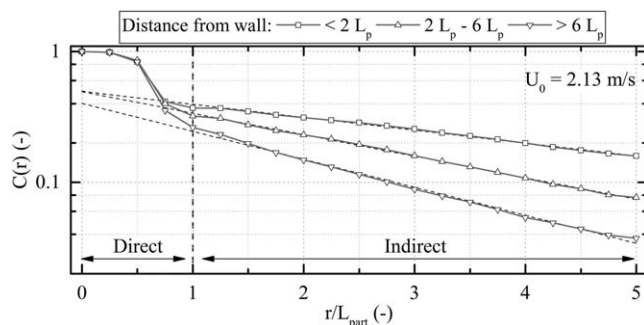


Figure 24. Spatial autocorrelation results for the large bed at $U_0=2.13$ m/s.

Symbols with gray solid lines represent measured data, dashed lines show the fitted exponential decay (Eq. 13). From the intercept of the line a_{pre} is calculated, from the slope λ is acquired.

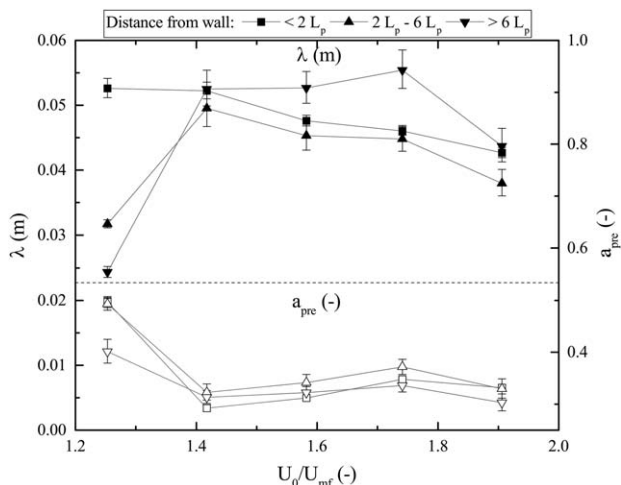


Figure 25. Correlation length (top, left scale) and pre-exponential factor (bottom, right scale).

Error bars represent 95% confidence intervals.

where orientation is random beyond the particle length. This behavior is expected for very dilute particles (high void fraction).

Figure 25 shows the found correlation lengths, and pre-exponential factors. At the lowest flow rate, still partially in the channeling regime, there is a high correlation length near the wall and a much lower value in the bulk. This is explained by the fact that channels form mainly in the center of the bed, not near the wall. At this flow rate, the prefactor shows that indirect interaction (stacking) is especially strong outside the channels, where particles are largely stationary, as is expected.

At higher gas velocities, the correlation length in the bulk increases, and then suddenly drops. Possibly, this is caused by interlocking behavior (packed groups of particles moving up through the center, then breaking up and raining down), which disappears at the highest flow rate. This is supported by the drop in prefactor at the highest flow rate, which suggests that particles are less packed. However, to fully understand this effect, more measurements are needed.

Particle coordination number

Figure 26 shows the average particle coordination number as a function of the average vertical velocity in the frame. The coordination number (CN) is defined here as the number of neighbors in a $2L_p \times 2L_p$ area around the particle. The large bed was divided into four 15×15 cm sections (extending from the wall to the center of the bed and up to 60 cm height). Recordings were made at $U_0=2.5$ m/s and $U_0=3.0$ m/s, 15,000 frames were captured for each height in the bed.

At the lowest position, velocities are small (as also shown by PIV measurements) and the particles are generally densely packed. At the higher positions, a proportional relationship between CN and velocity is observed. It can also be seen that the distribution of velocities is not symmetric around zero. This means that the particles move up relatively slowly in the densely packed regions, and then rain down faster in the dilute regions. See Figure 11 for a qualitative picture of why these trends are seen.

When comparing the results at the two different flow rates, it is observed that at the higher flow rate, the velocity distribution is broader and the coordination number is generally

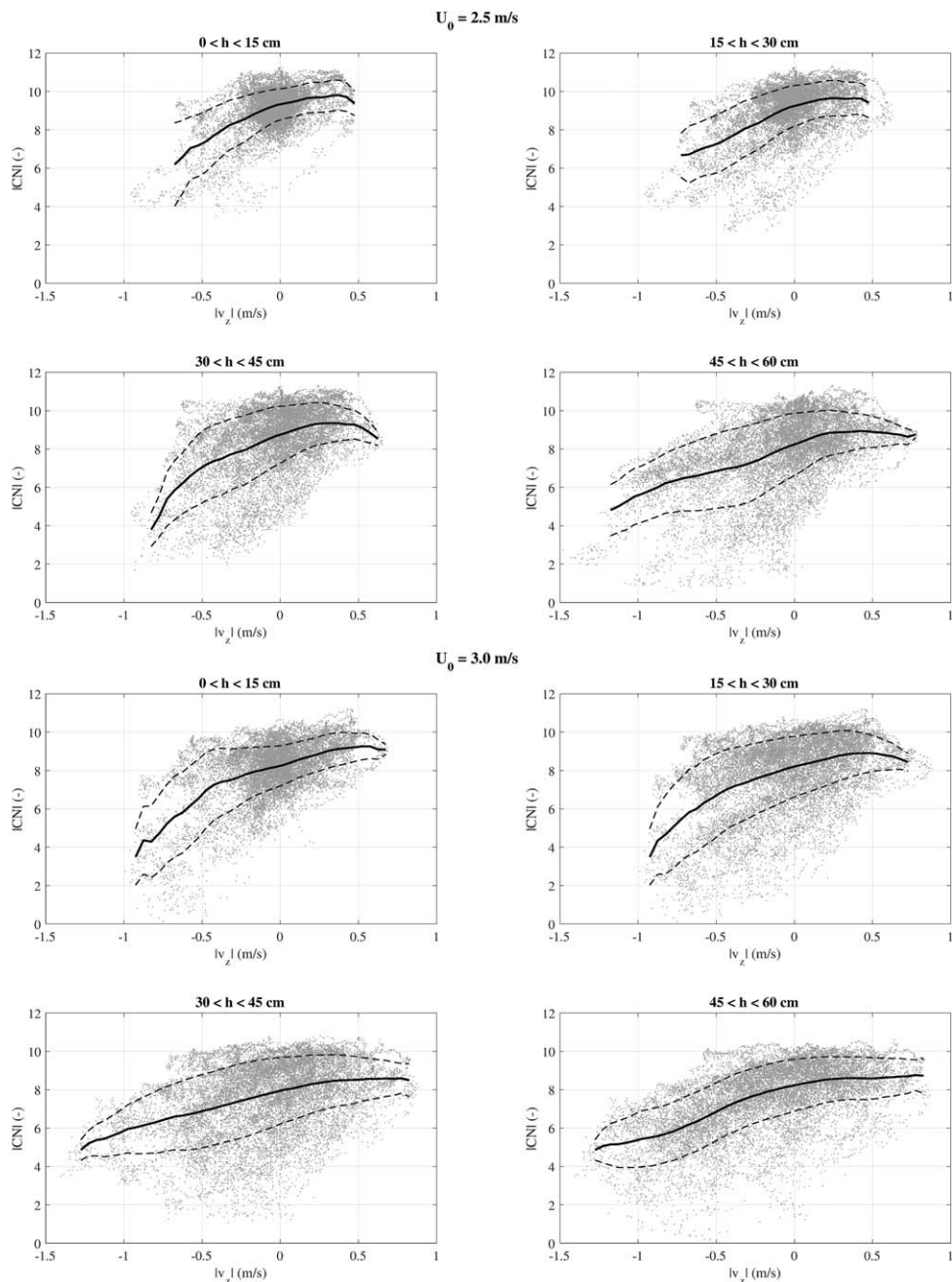


Figure 26. Average particle coordination number as a function of average vertical velocity, obtained from PTV measurements in the large bed at $U_0 = 2.5$ m/s (top) and $U_0 = 3.0$ m/s (bottom).

Points indicate individual frames, solid line gives the running average, dashed line shows the standard deviation.

slightly lower. This is in line with the observed break-down of the interlocking particle structures at high gas velocities.

Conclusions and Outlook

In this study, the fluidization behavior of elongated particles characterized as Geldart-D has been investigated experimentally. Pressure drop and bed height measurements in two different sized setups have shown that, based on gas velocity, different regimes can be defined. At low gas velocity, the particles are packed, but as the flow rate increases, channels form. First, there is so-called passive channeling, meaning that no particles move through the channels. In the large setup, at slightly higher gas velocity, active channeling was observed,

with particles flowing through the channels and forming fountains. Finally, well above the minimum fluidization velocity, the particles show bubbling fluidization. Even at the highest flow rates, particles show interlocking behavior, moving in large packed groups. It was demonstrated with experiments of two different sizes of rod-like particles and spherical particles that the behavior described above is entirely an effect of particle shape, rather than particle size or material.

A Digital Image Analysis algorithm has been developed to analyze the orientation of particles. It was shown that at low gas velocity, particles prefer to lie down horizontally, while at high flow rate the particles align themselves along the flow direction. A spatial autocorrelation analysis has been performed to investigate the coalignment of particles. The

orientation correlation length was shown to be in the order of 3–5 particle lengths. At low flow rates (channeling regime), there is a strong correlation near the walls and a very weak correlation in the bulk. At higher flow rates (bubbling fluidization) the correlation length is not dependent on position in the bed, and slowly decreases with increasing flow rate.

PIV has been applied to study the solid phase velocity and mass flux in the bed. A void fraction calculation algorithm based on CFD-DEM simulation data is used to obtain 3D void fractions. At sufficiently high flow rates, a circulation pattern similar to what is commonly observed for spherical particles is found. Particles generally move up through the center of the bed, and come down along the walls. To gain knowledge on individual particles, PTV has been used. By analyzing the number of nearest neighbors (coordination number) for each particle, it was shown that particles tend to move up slowly in densely packed groups and rain down faster in dilute regions.

It is also possible to measure rotational velocities of the non-spherical particles. However, there are a few difficulties in doing this. Due to the nature of fluidization of elongated particles, we see particle-particle interaction as a dominant factor, as also observed for other dense gas–solid system. This leads to bulk behavior that is, blocks of particles moving together, demonstrated by our PTV results. This leaves a low amount of rotational freedom, rendering this analysis unattractive. To be able to measure the rotational velocity it is important to sample sufficiently long trajectories. However, it is highly unlikely that individual particles stay and rotate in the plane parallel to the front wall. Also, particles are in the captured frame only for a very short amount of time especially for particles that are raining down.

Results on particle orientation and co-ordination numbers from this experimental study can have significant implications for both particle-scale and laboratory-scale numerical studies. In the case of particle-scale simulations, using a direct numerical simulation such as the lattice Boltzmann method,⁵⁰ the choice of particular arrangements, in terms of volume fraction of particles and relative orientation to a fluid flow, will directly influence the measured hydrodynamic response. Experiments can be used to dictate the choice of particle arrangements to ensure that simulations consider arrangements that are representative of real fluidized systems. At the laboratory scale, where particle dynamics can be simulated using a CFD-DEM approach,⁵¹ experimental data sets such as those presented in this study are invaluable with regards to validating and adjusting simulations. Given the anisotropic geometry of the particles in this study, hydrodynamic forces other than drag such as torque and lift are of relevance. Simulation output for various hydrodynamic relations included in CFD-DEM simulations can be compared with experiments to test the validity of these relations.

Acknowledgments

The authors thank the European Research Council for its financial support under its consolidator grant scheme, contract no. 615096 (NonSphereFlow). FP7 Ideas: European Research Council, 615096 (NonSphereFlow).

Nomenclature

Greek symbols

- α = Orientation, deg
- ϵ = Void fraction, -
- η = Dynamic viscosity, Pa·s
- λ = Correlation length, m
- ϕ = Sphericity, -

- ϕ_m = Mass flux, kg/m²s
- ρ = Density, kg/m³

Roman symbols

- A = Surface area, m²
- A_f, B_f = Fitting parameters, -
- a_{pre} = Pre-exponential factor, -
- D = Hydraulic diameter, m
- f_s = Solids volume fraction, -
- g = Gravity, m/s²
- L_p = Particle length, m
- M = Mass, kg
- N = Number, -
- P = Pressure, Pa
- R² = Coefficient of determination, -
- S = Standard deviation, Pa
- U = Superficial gas velocity, m/s
- V = Volume, m³
- v = Particle velocity, m/s
- y_i = Measured values, Pa
- Re = Reynolds number, -

Subscripts

- mf = Minimum fluidization
- SV = Surface volume equivalent

References

1. Rapagna S, Jand N, Kiennemann A, Foscolo P. Steam-gasification of biomass in a fluidised-bed of olivine particles. *Biomass Bioenergy*. 2000; 19(3):187–197.
2. Zhong W, Yu A, Liu X, Tong Z, Zhang H. Dem/cfd-dem modelling of non-spherical particulate systems: theoretical developments and applications. *Powder Technol.* 2016;302:108–152.
3. Zastawny M, Mallouppas G, Zhao F, van Wachem B. Derivation of drag and lift force and torque coefficients for non-spherical particles in flows. *Int J Multiphase Flow*. 2012;39:227–239.
4. Hölzer A, Sommerfeld M. New simple correlation formula for the drag coefficient of non-spherical particles. *Powder Technol.* 2008; 184(3):361–365.
5. Zhou ZY, Pinson D, Zou RP, Yu AB. Discrete particle simulation of gas fluidization of ellipsoidal particles. *Chem Eng Sci*. 2011;66(23): 6128–6145.
6. Deen NG, Van Sint Annaland M, Van der Hoef MA, Kuipers JAM. Review of discrete particle modeling of fluidized beds. *Chem Eng Sci*. 2007;62(1–2):28–44.
7. Goldschmidt MJV, Link JM, Mellema S, Kuipers JAM. Digital image analysis measurements of bed expansion and segregation dynamics in dense gas-fluidised beds. *Powder Technol.* 2003;138(2–3):135–159.
8. Jong JFD, Odu SO, Buijtenen MSV, Deen NG, Annaland MVS, Kuipers JAM. Development and validation of a novel Digital Image Analysis method for fluidized bed Particle Image Velocimetry. *Powder Technol.* 2012;230:193–202.
9. Zhong WQ, Zhang Y, Jin BS, Zhang MY. Discrete element method simulation of cylinder-shaped particle flow in a gas-solid fluidized bed. *Chem Eng Technol.* 2009;32(3):386–391.
10. Vollmari K, Oschmann T, Wirtz S, Kruggel-Emden H. Pressure drop investigations in packings of arbitrary shaped particles. *Powder Technol.* 2015;271:109–124.
11. Vollmari K, Jasevicius R, Kruggel-Emden H. Experimental and numerical study of fluidization and pressure drop of spherical and non-spherical particles in a model scale fluidized bed. *Powder Technol.* 2016;291:506–521.
12. Liu B, Zhang X, Wang L, Hong H. Fluidization of non-spherical particles: Sphericity, Zingg factor and other fluidization parameters. *Particuology*. 2008;6(2):125–129.
13. Liu L, Litster J. The effect of particle shape on the spouting properties of non-spherical particles. *Powder Technol.* 1991;66(1):59–67.
14. Cai J, Li Q, Yuan Z. Orientation of cylindrical particles in gas-solid circulating fluidized bed. *Particuology*. 2012;10(1):89–96.
15. Boyce CM, Rice NP, Ozel A, Davidson JF, Sederman AJ, Gladden LF, Sundaresan S, Dennis JS, Holland DJ. Magnetic resonance characterization of coupled gas and particle dynamics in a bubbling fluidized bed. *Phys Rev Fluids*. 2016;1(7):074201.

16. Buist KA, van der Gaag AC, Deen NG, Kuipers JAM. Improved magnetic particle tracking technique in dense gas fluidized beds. *AIChE J.* 2014;60(9):3133–3142.
17. Chaouki J, Larachi F, Duduković MP. Noninvasive tomographic and velocimetric monitoring of multiphase flows. *Ind Eng Chem Res.* 1997;36(11):4476–4503.
18. Yang Z, Fan X, Fryer P, Parker D, Bakalis S. Improved multiple-particle tracking for studying flows in multiphase systems. *AIChE J.* 2007;53(8):1941–1951.
19. Shao Y, Ren B, Jin B, Zhong W, Hu H, Chen X, Sha C. Experimental flow behaviors of irregular particles with silica sand in solid waste fluidized bed. *Powder Technol.* 2013;234:67–75.
20. Escudie R, Epstein N, Grace J, Bi H. Effect of particle shape on liquid-fluidized beds of binary (and ternary) solids mixtures: segregation vs. mixing. *Chem Eng Sci.* 2006;61(5):1528–1539.
21. Gabitto J, Tsouris C. Drag coefficient and settling velocity for particles of cylindrical shape. *Powder Technol.* 2008;183(2):314–322.
22. Ergun S. Fluid flow through packed columns. *Chem Eng Prog.* 1952;48:89–94.
23. Metha D, Hawley MC. Wall effect in packed columns. *Ind Eng Chem Process Des Dev.* 1969;8(2):280–282.
24. Foumeny E, Benyahia F, Castro J, Moallemi H, Roshani S. Correlations of pressure drop in packed beds taking into account the effect of confining wall. *Int J Heat Mass Transf.* 1993;36(2):536–540.
25. Reichelt W. Zur Berechnung des Druckverlustes einphasig durchströmter Kugel und Zylinder Schüttungen. *Chem Ing Tech.* 1972;44(18):1068–1071.
26. Liu S, Masliyah JH. Single fluid flow in porous media. *Chem Eng Commun.* 1996;148–150(1):653–732.
27. Raichura RC. Pressure drop and heat transfer in packed beds with small tube-to-particle diameter ratio. *Exp Heat Transf.* 1999;12(4):309–327.
28. Montillet A, Akkari E, Comiti J. About a correlating equation for predicting pressure drops through packed beds of spheres in a large range of Reynolds numbers. *Chem Eng Process Process Intensification.* 2007;46(4):329–333.
29. Cheng NS. Wall effect on pressure drop in packed beds. *Powder Technol.* 2011;210(3):261–266.
30. Gibilaro LG. *Fluidization-Dynamics: The Formulation and Applications of a Predictive Theory for the Fluidized State*, 1 ed. Oxford: Butterworth-Heinemann, 2001.
31. Nemeč D, Levec J. Flow through packed bed reactors: 1. Single-phase flow. *Chem Eng Sci.* 2005;60(24):6947–6957.
32. Allen KG, von Backström TW, Kröger DG. Packed bed pressure drop dependence on particle shape, size distribution, packing arrangement and roughness. *Powder Technol.* 2013;246:590–600.
33. Singh R, Saini RP, Saini JS. Nusselt number and friction factor correlations for packed bed solar energy storage system having large sized elements of different shapes. *Sol Energy.* 2006;80(7):760–771.
34. Einfeld B, Schnitzlein K. The influence of confining walls on the pressure drop in packed beds. *Chem Eng Sci.* 2001;56(14):4321–4329.
35. Busciglio A, Vella G, Micale G, Rizzuti L. Analysis of the bubbling behaviour of 2D gas solid fluidized beds. Part I. Digital image analysis technique. *Chem Eng J.* 2008;140(1–3):398–413.
36. Shen L, Johnsson F, Leckner B. Digital image analysis of hydrodynamics two-dimensional bubbling fluidized beds. *Chem Eng Sci.* 2004;59(13):2607–2617.
37. Warr S, Jacques GTH, Huntley JM. Tracking the translational and rotational motion of granular particles: use of high-speed photography and image processing. *Powder Technol.* 1994;81(1):41–56.
38. Duda RO, Hart PE. Use of the Hough transform to detect lines and curves in pictures. *Commun Assoc Comput Mach.* 1972;15(1):11–15.
39. McLaughlin R. Randomized Hough Transform: improved ellipse detection with comparison. *Pattern Recognit Lett.* 1998;19(3–4):299–305.
40. Olaofe OO, Buist KA, Deen NG, van der Hoef MA, Kuipers JAM. Improved digital image analysis technique for the evaluation of segregation in pseudo-2D beds. *Powder Technol.* 2013; 244:61–74.
41. van Buijtenen MS, Börner M, Deen NG, Heinrich S, Antonyuk S, Kuipers JAM. An experimental study of the effect of collision properties on spout fluidized bed dynamics. *Powder Technol.* 2011; 206(1–2):139–148.
42. Stukowski A. Visualization and analysis of atomistic simulation data with OVITO—the Open Visualization Tool. *Model Simul Mater Sci Eng.* 2010;18(1):015012.
43. Adrian RJ, Westerweel J. *Particle Image Velocimetry*, 1 ed. Cambridge: Cambridge University Press, 2011.
44. Kruggel-Emden H, Vollmari K. Flow-regime transitions in fluidized beds of non-spherical particles. *Particuology.* 2015;29:1–15.
45. Wang Z, Kwauk M, Li H. Fluidization of fine particles. *Chem Eng Sci.* 1998;53(3):377–395.
46. Kunii D, Levenspiel O. *Fluidization Engineering*, 2nd ed. Butterworth-Heinemann, a division of Reed Publishing Inc., 1991. doi: 10.1016/B978-0-08-050664-7.50003-2. Available at <https://www.elsevier.com/books/fluidization-engineering/brenner/978-0-08-050664-7>.
47. Geldart D. *Gas Fluidization Technology*, 1st ed. New York: John Wiley & Sons Ltd., 1986.
48. Howard J. *Fluidized Beds Combustion and Application*, 1st ed. Barking, England: Applied Science Publishers Ltd, 1983.
49. Geldart D. Types of gas fluidization. *Powder Technol.* 1973;7(5): 285–292.
50. Sanjeevi SKP, Padding JT. On the orientational dependence of drag experienced by spheroids. *J Fluid Mech.* 2017;820:R1.
51. Mema I, Mahajan VV, Fitzgerald BW, Kuipers H, Padding JT. Effect of lift force on dense gas-fluidized beds of non-spherical particles. In: *12th International Conference on CFD in Oil & Gas, Metallurgical and Process Industries*, Trondheim. 2017.

Manuscript received Sep. 26, 2017, and revision received Dec. 19, 2017.